Director gliding in a nematic liquid crystal layer: Quantitative comparison with experiments

E. Mema, L. Kondic, and L. J. Cummings

Phys. Rev. E **97**, 032704 — Published 19 March 2018

DOI: 10.1103/PhysRevE.97.032704

Director gliding in a nematic liquid crystal layer: Quantitative comparison with experiments

E. Mema,[1,*] L. Kondic,[1] and L.J. Cummings[1]

[1] *Department of Mathematical Sciences and Center for Applied Mathematics and Statistics New Jersey Institute of Technology, Newark, NJ 07102*

The interaction between nematic liquid crystals and polymer-coated substrates may lead to slow reorientation of the easy axis (so called "director gliding") when a prolonged external field is applied. We consider the experimental evidence of zenithal gliding observed by Joly *et al.* in Phys. Rev. E **70**, (2004) and Buluy *et al.* in J. Soc. Inf. Disp. **14**, (2006) as well as azimuthal gliding observed by S. Faetti and P. Marianelli in Liq. Cryst. **33**, (2006) and present a simple, physically-motivated model that captures the slow dynamics of gliding both in the presence of an electric field and after the electric field is turned off. We make a quantitative comparison of our model results and the experimental data and conclude that our model explains the gliding evolution very well.

I. INTRODUCTION

Liquid crystal display (LCD) devices make up a large portion of the electronic devices in today's market due to their high optical resolution screens. A typical LCD consists of many pixels, each consisting of a layer of nematic liquid crystal (NLC) sandwiched between two bounding plates and crossed polarizers. These devices exploit the NLC's ability to rotate the plane and shift the phase of polarized light, to generate two distinct optical configurations. The "bright" and "dark" pixels of the display are a result of the different orientation of LC molecules within the layer. The molecular orientation depends on the boundary conditions at the plates as well as the external forces (usually an applied electric field). To give a simplified explanation (for brevity): when an electric field is applied across the layer, the LC molecules align with the field and cannot rotate the polarized light beam, so that it cannot pass the second (crossed) polarizer and the pixel remains "dark". On the contrary, if no electric field is applied, the LC molecules have a preferred orientation dictated by the boundary conditions that allows the polarized light beam to be rotated so that it passes the second crossed polarizer, forming a "bright" pixel in the display.

In an effort to improve LCD design and function, much research has been focused on understanding and controlling the interaction between the bounding surfaces and the liquid crystal molecules, known as *anchoring*. As noted above, the molecules have a preferred orientation at the boundary plates, often dictated by the substrate coating material and different mechanical and/or chemical treatments. Anchoring may be weak or strong. In both cases, the substrate is characterized by an "easy axis", the axis along which the interaction energy between the substrate and liquid crystal molecules is minimized. If anchoring is strong, the NLC molecules align nearly parallel to the easy axis at the boundary. If anchoring is weak, the NLC molecules may deviate from the easy axis, generating a surface and elastic torque, which balance. Experiments have shown that if a strong applied torque exists for extended periods of time, the easy axis can slowly rotate, leading to a phenomenon known as *easy axis gliding* or *director gliding* [1] (the director is a unit vector characterizing the average molecular orientation of the long axis of the molecules). Director gliding has been observed in lyotropic, thermotropic and nematic LCs with multiple experiments reporting both zenithal and azimuthal gliding [1–8].

Understanding the mechanism behind director gliding is important since it is believed to lead to "image sticking" in LCD technology. Image sticking is a phenomenon where an outline (ghost image) of a previously displayed image remains visible on an LCD screen after the image has been removed [9]. Director gliding may also pose a challenge in the development of flexible LCDs since experiments have shown that director gliding is more prevalent at LC-polymer interfaces, often present in flexible LCDs.

Two mechanisms have been proposed to describe the gliding phenomenon observed in experiments. The first, introduced by Vetter *et al.* [5], describes gliding in terms of adsorption/desorption of the LC molecules on the solid substrate as follows: initially the LC molecules are adsorbed along the direction of the director in the cell. As an electric field is applied across the layer, the director reorients according to the electric field, leading to the adsorption of LC molecules along this new direction. As a consequence, the symmetry axis of the angular distribution function of the adsorbed molecules reorients, together with the associated easy axis [10].

The second mechanism, proposed by Kurioz *et al.* [11], describes gliding as follows: due to weak anchoring imposed on the boundary, applying an electric field reorients the director on the surface, which drags the flexible fragments of the molecules in the polymer surface. This results in the reorientation of both the liquid crystal molecules and the flexible fragments with the rate determined by the anchoring strength and the liquid crystal-flexible fragment interaction. Both mechanisms present

* **Current Affiliation:** Department of Mathematics, College of Staten Island, City University of New York

the gliding phenomenon in a general way, but to our knowledge, have not been described by mechanistic predictive models.

In this paper, we discuss experiments that present both azimuthal and zenithal gliding. In the case of zenithal gliding we consider two sets of experiments, carried out by Joly *et al.* [6] and Buluy *et al.* [10], that focus on zenithal gliding in the presence of an electric field and after the electric field is turned off. In the case of azimuthal gliding, we consider the experiment carried out by Faetti & Marianelli [12], which provides evidence for azimuthal director gliding of a strongly anchored system as an electric field is applied across the layer. Zenithal director gliding is observed as an electric field is applied perpendicular to the bounding plates [6] and after the applied electric field is removed [6, 10]. By contrast, azimuthal gliding is observed as an electric field is applied parallel to the plates [12].

All investigations present simple models used to obtain the best fit to each experiment. In Ref. [6], the authors argue that the director angle at the gliding substrate can be fitted by a sum of no fewer than three exponential terms, with the three exponents determined independently for field *on* and *off* cases (six exponents total). Buluy *et al.* [10] present a similar model but consisting of two exponential terms, chosen specifically to best fit the experimental data; while Faetti & Marianelli [12] compare the experimental results with a stretched exponential function and two fitting parameters.

In this paper, we develop mechanistic models that aim to capture the physics of the interaction between NLC molecules and the adjacent polymer coated boundary, and that explain the gliding data observed in all three sets of experiments. The paper is laid out as follows: in Sec. II A, we present the mathematical model that governs the evolution of the director field, coupled to two gliding models that capture the slow zenithal reorientation of the easy axis. Similarly, in Sec. II B, we present a mathematical model that captures the slow azimuthal reorientation of the easy axis as an electric field is applied across the layer, parallel to the bounding plates. Sections III A, III C and III E summarize the experimental data observed in [6, 10, 12] respectively, while Sections III B, III D and III F present the numerical results of our models and compare them to the experimental data. Section IV presents the conclusions.

II. MATHEMATICAL MODEL

In the following we develop mathematical models for director gliding for two simple cases in which the director field is confined to a plane (zenithal gliding, and azimuthal gliding). In both cases the slow timescale on which gliding operates (relative to the elastic response time of NLC molecules) will be exploited to derive a simplified quasistatic model. We address the case of zenithal gliding first.

A. Zenithal Molecular Orientation

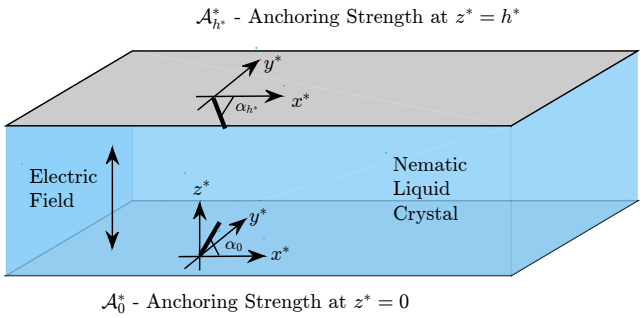

Figure 1: (Color online) Sketch showing the setup of the zenithal model.

The basic setup consists of a NLC layer bounded between two parallel plates shown in Fig. 1. The local average molecular orientation can be described by a unit vector *director* field $\boldsymbol{n}$. Since the experimental data considered in [6, 10] describe zenithal gliding, we assume that the director field lies in the (x^*, z^*) plane, with its properties varying in the z^* direction only (the direction perpendicular to the bounding plates). Here $*$ is used to denote dimensional quantities; unstarred quantities introduced later will be dimensionless. Hence, the director $\boldsymbol{n} = (\cos\theta, 0, \sin\theta)$ can be written in terms of a single angle $\theta(z^*)$. An electric field $\mathbf{E}^*$ is applied perpendicular to the bounding plates and is assumed to be uniform throughout the layer: $\mathbf{E}^* = E^*(0, 0, 1)$. In reality, the NLC molecules interact with the field, leading to gradients in the field, but in many practical situations such gradients may be shown to be small [13] and we assume this is the case here.

Our mathematical model is based on the Ericksen-Leslie continuum theory of nematics [14–16] where the total free energy density of the liquid crystal layer consists of the bulk and surface energy densities, both functions of the director orientation, $\boldsymbol{n}$. With the above assumptions, the total free energy per unit area is given by:

$$J^* = \int_0^{h^*} W^* dz^* + g^*_0|_{z^*=0} + g^*_{h^*}|_{z^*=h^*}, \qquad (1)$$

where W^* is the bulk energy density and $g^*_{\{0,h^*\}}$ are the Rapini-Papoular surface energies at boundaries $z^* = 0, h^*$ given by:

$$W^* = \frac{K^*}{2}\theta^2_{z^*} - \frac{E^{*2}\varepsilon^*_0(\varepsilon_\parallel - \varepsilon_\perp)}{2}\sin^2\theta \qquad (2)$$
$$- \frac{E^*(e^*_1 + e^*_3)}{2}\theta_{z^*}\sin 2\theta,$$

$$g^*_{\{0,h^*\}} = \frac{\mathcal{A}^*_{\{0,h^*\}}}{2}\sin^2(\theta - \alpha_{\{0,h^*\}}). \qquad (3)$$

Here, K^* represents the single elastic constant of the NLC, under the frequent assumption that the bend and splay elastic constants are equal in magnitude (i.e. $K^* = K_1^* = K_3^*$). The parameter $\varepsilon_0^* = 8.854 \times 10^{-12}$ $\mathrm{C^2N^{-1}m^{-2}}$ represents the permittivity of free space, while $\varepsilon_\parallel$ and $\varepsilon_\perp$ are the relative dielectric permittivities parallel and perpendicular to the long axis of the nematic molecules, and e_1^* and e_3^* are the flexoelectric coefficients, different for each liquid crystal type. In the following, however, we will omit this flexoelectric contribution from the model, noting that in the one dataset we compare to with an applied field [6], the experiments use a high-frequency AC power supply, so that over the relevant experimental timescales the flexoelectric terms in the model will average to zero. For the dielectric contribution, we consider the common case in which the LC molecules align parallel with the electric field (rather than perpendicular to it) since the LC material 5CB used in Refs. [6, 10] has a positive dielectric coefficient, $\varepsilon_\parallel - \varepsilon_\perp > 0$. The parameters $\mathcal{A}^*_{\{0,h^*\}}$ represent the anchoring strengths associated with each boundary, while $\alpha_{\{0,h^*\}}$ are the preferred zenithal anchoring angles at $z^* = 0, h^*$ boundary (see Figure 1). Following the approach adopted in [13, 17–19], we assume that the system evolves as a gradient flow to its total free energy minimum, leading to the following time dependent problem:

$$\mu^*\theta_{t^*} = K^*\theta_{z^*z^*} + \frac{\varepsilon_0^*(\varepsilon_\parallel - \varepsilon_\perp)E^{*2}}{2}\sin 2\theta, \tag{4}$$

$$\tilde{\nu}^*\theta_{t^*} = K^*\theta_{z^*} - \frac{\mathcal{A}_0^*}{2}\sin 2(\theta - \alpha_0)\Big|_{z^*=0}, \tag{5}$$

$$-\tilde{\nu}^*\theta_{t^*} = K^*\theta_{z^*} + \frac{\mathcal{A}_{h^*}^*}{2}\sin 2(\theta - \alpha_{h^*})\Big|_{z^*=h^*}, \tag{6}$$

where μ^* and $\tilde{\nu}^*$ represent the bulk and surface rotational viscosities, respectively. In the following section, we briefly discuss the model for azimuthal molecular orientation.

B. Azimuthal Molecular Orientation

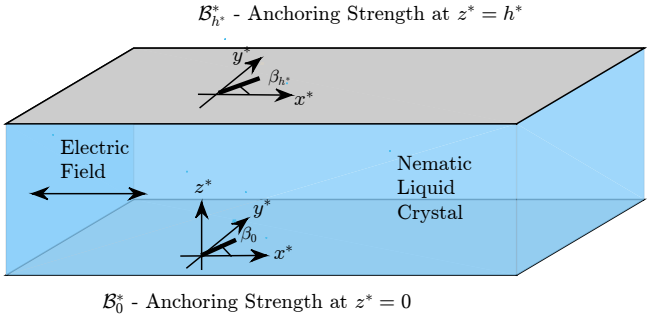

Figure 2: (Color online) Sketch showing the setup of the azimuthal model.

The basic setup for an azimuthal model, shown in Fig. 2, consists of a NLC layer bounded between two parallel plates where the local average molecular orientation can be described by a unit vector $\boldsymbol{n}$, and anchoring is planar. Faetti & Marianelli [12] consider a NLC layer bounded by two nearly parallel plates creating a wedge cell of shallow angle. In our model, we assume that the two bounding plates are exactly parallel, one plate occupying the (x^*, y^*)-plane, and that the director field lies in a plane parallel to this plane, its properties varying in the z^* direction only. Hence, the director $\boldsymbol{n} = (\cos\phi, \sin\phi, 0)$ can be written in terms of a single angle, $\phi(z^*)$. A uniform electric field is applied parallel to the bounding plates and nearly perpendicular to the x^*-axis: $\mathbf{E}^* = E^*(\cos 85°, \sin 85°, 0)$.

As with the zenithal model, we base the azimuthal model on the free energy density given in Eq. (1). Here, however, W^* and $g_{\{0,h^*\}}$ take the following form:

$$W^* = \frac{K^*}{2}\phi_{z^*}^2 - \frac{E^{*2}\varepsilon_0^*(\varepsilon_\parallel - \varepsilon_\perp)}{2}\cos^2(\phi - 85°),$$

$$g^*_{\{0,h^*\}} = \frac{\mathcal{B}^*_{\{0,h^*\}}}{2}\sin^2(\phi - \beta_{\{0,h^*\}}),$$

where $\mathcal{B}^*_{\{0,h^*\}}$ represent the anchoring strengths associated with each boundary while $\beta_{\{0,h^*\}}$ are the preferred azimuthal anchoring angles at $z^* = 0, h^*$, and all other parameters are as defined previously. Again, assuming evolution via a gradient flow to the total free energy minimum, we obtain the following time dependent problem, analogous to Eqs. (4)–(6):

$$\mu^*\phi_{t^*} = K^*\phi_{z^*z^*} + \frac{\varepsilon_0^*(\varepsilon_\parallel - \varepsilon_\perp)E^{*2}}{2}\sin 2(\phi - 85°), \tag{7}$$

$$\tilde{\nu}^*\phi_{t^*} = K^*\phi_{z^*} - \frac{\mathcal{B}_0^*}{2}\sin 2(\phi - \beta_0)\Big|_{z^*=0}, \tag{8}$$

$$-\tilde{\nu}^*\phi_{t^*} = K^*\phi_{z^*} + \frac{\mathcal{B}_{h^*}^*}{2}\sin 2(\phi - \beta_{h^*})\Big|_{z^*=h^*}, \tag{9}$$

where μ^* and $\tilde{\nu}^*$ represent the bulk and surface rotational viscosities, respectively. In the following section, we supplement Eqs. (4)–(6) and Eqs. (7)–(9) with additional models designed to capture the slow molecular reorientation at the boundary under the gliding process for both zenithal and azimuthal models. We then proceed by introducing the scales used to nondimensionalize the models.

C. Gliding

The orientation that NLC molecules adopt at a polymer-coated boundary depends on several factors, including: the preferred molecular orientation at the boundary (the easy axis, also known as the anchoring direction); the anchoring strength at the boundary; anchoring conditions at other nearby boundaries, which can induce bulk elastic distortions leading to molecular torques

at interfaces; and any other external forces (such as an applied electric field). At a nongliding surface, the preferred orientation (easy axis) is a fixed property of the NLC-surface pair, while at a gliding surface, the easy axis can slowly reorient in time. The slow reorientation occurs due to a sustained torque on the substrate molecules, created (for example) by a prolonged exposure to an applied electric field [2–5, 7, 8, 20, 21], or due to internal elastic stresses created by different anchoring properties at the two boundaries of a confined layer [22]. The (simplified) physical picture we have in mind is that the surface substrate molecules (those in contact with the NLC) experience competing forces: on one hand they are bound within the substrate; while on the other hand they interact with the molecules of the adjacent NLC. At a nongliding surface, the former forces are fully dominant and the surface substrate molecules remain firmly fixed. At a gliding surface however, the forces due to the NLC interactions can be significant, and over timescales of minutes to hours, can reorient the surface substrate molecules, leading to an attendant change in the direction of the easy axis.

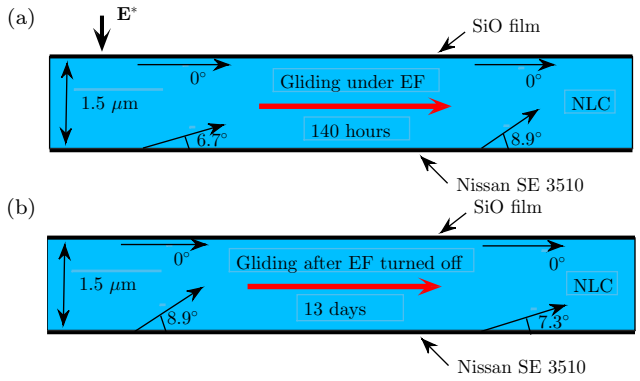

Figure 3: (Color online) Schematic summarizing the drift of the easy axis (gliding) at the lower substrate in [6] (a) during the time of application of an electric field; and (b) after the electric field is turned off. Anchoring angles in this and following figures are not drawn to scale.

Figure 3 summarizes the zenithal gliding observed by Joly *et al.* [6]. Under prolonged application of an applied field, these authors tracked the evolution of the easy axis at the lower surface (Nissan SE 3510), observing that its angle increases from its initial value (Fig. (3a)). After the electric field is turned off, the easy axis at this surface is tracked again, and is observed to glide back almost to its initial position (Fig. (3b)).

Similarly, Fig. 4 schematizes the experimental procedure of Buluy *et al.* [10]. An electric field is applied continuously across a layer, causing the anchoring angle at the lower substrate (PVCN-F) to begin to deviate (glide) from its preferred orientation. After the electric field is removed, the anchoring angle glides back toward its initial position.

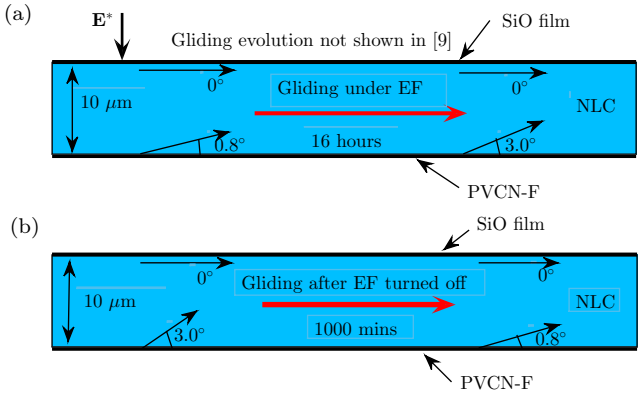

Figure 4: (Color online) Schematic summarizing the drift of the easy axis (gliding) at the lower substrate in [10] (a) during the time of application of an electric field; and (b) after the electric field is turned off. As indicated, the authors do not provide data on the initial gliding dynamics under the applied electric field.

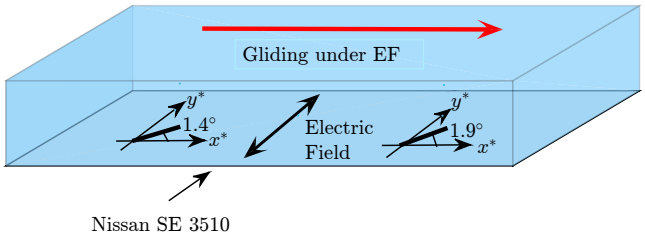

Figure 5: (Color online) Schematic summarizing the drift of the easy axis (gliding) in [12] during the application of an electric field.

The experiment described in [12] consists of a slightly different setup, shown in Fig. 5. Here, an electric field is applied parallel to the bounding plates, at an angle of 85° from the x^*-axis. The preferred anchoring angles at the gliding surface are parallel to the x^*-axis. Upon application of the electric field the authors report an immediate jump of the easy axis, followed by a gradual increase, attributed to gliding.

We propose two models to describe the gliding behavior observed in Refs [6, 10, 12], assuming in all cases that gliding occurs at the surface $z^* = 0$. In the following presentation we assume the zenithal anchoring case, and later make the natural extension to the azimuthal case. Both gliding models assume the same basic principle: that the direction of the easy axis at the gliding substrate is determined by how the substrate molecules are anchored. If we think of the substrate molecules as able to rotate slowly under torque, then the easy axis can rotate also (gliding). Considerations of force-balance for the substrate molecules on the timescales appropriate for gliding give that the torques acting on them should equilibrate. We assume two sources of torque: (i) a net force due to the interactions with the adjacent NLC molecules which, we posit, should be a function of $(\alpha_0(t^*) - \theta(0, t^*))$

(the difference between the easy axis and the director angles at that surface); and (ii) a resistive force. It is reasonable to assume that the resistive force is an increasing function of the rate of gliding, $d\alpha_0/dt^*$; lacking detailed data to support a better model we assume linear dependence. These considerations lead to a general gliding law of the form

$$\frac{d\alpha_0}{dt^*} = f(\alpha_0(t^*) - \theta(0,t^*)).$$

We consider two choices for the function f, motivated by the experimental observations:

$$\frac{d\alpha_0}{dt^*} = \lambda_0^*[\alpha_0(t^*) - \theta(0,t^*)]\left(1 - \frac{|\alpha_0(t^*) - \alpha_0(0)|}{\alpha_{\rm tol}}\right)^n \qquad \text{(Gliding Model I)}, \tag{10}$$

and

$$\frac{d\alpha_0}{dt^*} = \lambda_0^*[\alpha_0(t^*) - \theta(0,t^*)]\exp\left(-\frac{|\alpha_0(t^*) - \alpha_0(0)|}{\bar{\alpha}_{\rm tol}}\right) \qquad \text{(Gliding Model II)}. \tag{11}$$

Both models assume that the gliding force on the substrate molecules is as though they are tethered by springs to the adjacent NLC molecules: for small displacements the force is linear in the difference between anchoring angle and NLC orientation angle, but for larger displacements the driving torque decreases. This is in line with the experimental data, which strongly suggest that the degree of gliding that can occur is limited. In the first model, Eq. (10), we impose a maximal gliding angle $\alpha_{\rm tol}$, while in the second model, Eq. (11), we assume the existence of some angle $\bar{\alpha}_{\rm tol}$, below which gliding follows an approximately linear model, and above which the torque driving gliding drops rapidly. The exponent n in the first model allows the degree of nonlinearity to be tuned to fit the data. As one might anticipate, the two models display similar behavior as n becomes large as we will see in Sec. III; indeed, we find that large n is necessary for the model to fit well the data. The parameter λ_0^* in both models represents the relaxation rate of the anchoring angle at the gliding surface $z^* = 0$.

We note that the same principles used to derive Eqs. (10)–(11) can be extended to the azimuthal case. To model azimuthal gliding, we replace the zenithal anchoring angles $\alpha_{\{0,h^*\}}$ with the azimuthal anchoring angles $\beta_{\{0,h^*\}}$, the zenithal director angle $\theta(\cdot,t^*)$ with the azimuthal director angle $\phi(\cdot,t^*)$ and parameters $\alpha_{\rm tol}$, $\bar{\alpha}_{\rm tol}$ with the corresponding parameters $\beta_{\rm tol}$, $\bar{\beta}_{\rm tol}$.

D. Scaling and Nondimensionalization

We nondimensionalize Eqs. (4)–(6) (zenithal) and Eqs. (7)–(9) (azimuthal) as follows:

$$z = \frac{z^*}{h^*}, \quad t = \lambda_0^* t^*, \quad (\mathcal{A},\mathcal{B})_{\{0,1\}} = \frac{h^*}{K^*}(\mathcal{A}^*,\mathcal{B}^*)_{\{0,h^*\}} \tag{12}$$

where h^* is the thickness of the NLC layer which varies depending on the experimental setup. Note that time is scaled using the gliding timescale, $(\lambda_0^*)^{-1}$. This parameter will depend on system characteristics such as substrate material, treatment, and the NLC used. We note also that the applied field may affect not only the orientation of the NLC molecules, but also that of the polymer molecules in the coating layer (the material used to coat the gliding surface in [6] is the polyimide Nissan SE 3510, which has a dielectric constant of approximately 3.0). Therefore, we allow different values (based on the experimental data) for λ_0^* in "field on" and "field off" cases. After nondimensionalization, Eqs. (4)–(6) become:

$$\delta\theta_t = \theta_{zz} + \mathcal{D}\sin 2\theta, \tag{13}$$

$$\delta\tilde{\nu}\theta_t = \theta_z - \frac{\mathcal{A}_0}{2}\sin 2(\theta - \alpha_0) \quad \text{on} \quad z = 0, \tag{14}$$

$$-\delta\tilde{\nu}\theta_t = \theta_z + \frac{\mathcal{A}_1}{2}\sin 2(\theta - \alpha_1) \quad \text{on} \quad z = 1, \tag{15}$$

and Eqs. (7)–(9) read as:

$$\delta\phi_t = \phi_{zz} + \mathcal{D}\sin 2\phi, \tag{16}$$

$$\delta\tilde{\nu}\phi_t = \phi_z - \frac{\mathcal{B}_0}{2}\sin 2(\phi - \beta_0) \quad \text{on} \quad z = 0, \tag{17}$$

$$-\delta\tilde{\nu}\phi_t = \phi_z + \frac{\mathcal{B}_1}{2}\sin 2(\phi - \beta_1) \quad \text{on} \quad z = 1. \tag{18}$$

The parameter $\delta = ({h^*}^2\mu^*\lambda_0^*)/K^*$ in Eqs. (13)–(18) represents the ratio between the timescales of the bulk elastic response of the NLC, given by ${h^*}^2\mu^*/K^*$ and the gliding response, $1/\lambda_0^*$. The parameter $\tilde{\nu} = \tilde{\nu}^*/(\mu^* h^*)$ represents the dimensionless surface viscosity, while $\mathcal{D}$ represents the dimensionless dielectric strength:

$$\mathcal{D} = \frac{{h^*}^2{E^*}^2\varepsilon_0^*(\varepsilon_\parallel - \varepsilon_\perp)}{2K^*}. \tag{19}$$

We consider the common case in which the NLC molecules align parallel to the electric field direction,

so the dielectric anisotropy is positive and $\mathcal{D} > 0$ in our model. With the following parameter values: $h^* \sim 1.5 - 10$ μm ($h = 1.5$ μm in [6] and $h = 10\mu$m in [10]), $K^* = 8 \times 10^{-12}$N, $\tilde{\mu}^* = 0.1$ N s m^{-2}, $\tilde{\nu}^* \sim 10^{-10}$ N s m^{-1} [23], and relaxation rates in the range of $0.3 - 3.7$ min^{-1} (based on the experimental data for zenithal gliding [6, 10]; see later Secs. III B and III D), we observe that $\delta \ll 1$ and $\tilde{\nu} \ll 1$. Furthermore, since the anchoring at the upper (non-gliding) boundary is much stronger than at the lower (gliding) boundary in both zenithal experiments [6, 10], we assume $\mathcal{A}_1 \gg 1$ (strong anchoring at the upper boundary). Together these assumptions give, to leading order in δ, $\tilde{\nu}$, $\mathcal{A}_1^{-1}$:

$$0 = \theta_{zz} + \mathcal{D} \sin 2\theta, \tag{20}$$

$$0 = \theta_z - \frac{\mathcal{A}_0}{2} \sin 2(\theta - \alpha_0) \quad \text{on} \quad z = 0, \tag{21}$$

$$\theta = \alpha_1 \quad \text{on} \quad z = 1. \tag{22}$$

In the azimuthal gliding setup of Faetti & Marianelli, both bounding surfaces experience gliding. With parameter values $h \approx 50$ μm in [12], $K^* = 8 \times 10^{-12}$N, $\tilde{\mu}^* = 0.1$ N s m^{-2}, $\tilde{\nu}^* \sim 10^{-10}$ N s m^{-1} [23], and relaxation rates $\lambda_0^* = 0.275$ min^{-1} (based on the experimental data [12]), $\delta \ll 1$ and $\tilde{\nu} \ll 1$. Hence Eqs. (16)–(18) become:

$$0 = \phi_{zz} + \mathcal{D} \sin 2\phi, \tag{23}$$

$$0 = \phi_z - \frac{\mathcal{B}_0}{2} \sin 2(\phi - \beta_0) \quad \text{on} \quad z = 0, \tag{24}$$

$$0 = \phi_z + \frac{\mathcal{B}_1}{2} \sin 2(\phi - \beta_1) \quad \text{on} \quad z = 1. \tag{25}$$

The dimensionless forms of Eq. (10) and Eq. (11) are:

$$\frac{d\alpha_0}{dt} = [\alpha_0(t^*) - \theta(0,t)] \left(1 - \frac{|\alpha_0(t^*) - \alpha_0(0)|}{\alpha_{\text{tol}}}\right)^n, \tag{26}$$

$$\frac{d\alpha_0}{dt} = [\alpha_0(t) - \theta(0,t)] \exp\left(-\frac{|\alpha_0(t) - \alpha_0(0)|}{\bar{\alpha}_{\text{tol}}}\right), \tag{27}$$

for zenithal gliding at $z = 0$, with analogous equations governing the gliding evolution of β_0 and β_1 in the azimuthal gliding case.

Equations (20)–(22) together with Eq. (26) or Eq. (27) make up the complete model that describes the evolution of the easy axis within a NLC layer where the molecules are allowed to bend and splay in the (x, z)–plane and where gliding can occur at $z = 0$. Similarly, Eqs. (23)–(25) together with the azimuthal versions of Eq. (26) or Eq. (27) (gliding imposed at both boundaries) make up the complete model that describes the evolution of the easy axis within a NLC layer where the molecules are allowed to twist about the z-axis, while confined to the (x, y)-plane, and where gliding can occur at both $z = 0$ and $z = 1$.

We solve each set of equations numerically by implementing the following procedure: first we solve Eqs. (20)–(22) (or Eqs. (23)–(25) in the azimuthal case) using the built-in MATLAB routine BVP4c to obtain a solution $\theta(\cdot, t)$ for the director angle. Then, we use this solution in Eq. (26) or Eq. (27) (or the corresponding azimuthal gliding models) to compute the anchoring angle α_0 (or $\beta_{\{0,1\}}$) at the next time step. This process is repeated until we have simulated the entire duration of the corresponding experiment.

III. RESULTS

In this Section, we first summarize briefly the experimental results presented in [6, 10, 12]. Then, we present our numerical results obtained by solving numerically Eqs. (20)–(27) and make direct comparisons with the experimental data.

A. Overview of experimental results presented in Ref. [6]

The experimental setup considered in [6] consists of a NLC layer bounded between two substrates treated such that the lower substrate exhibits gliding, while anchoring is strong and planar at the upper boundary. The initial preferred anchoring orientation at the gliding boundary is $\alpha_0 = 6.7°$, measured from the horizontal axis (Figure 3), before application of the electric field. Joly *et al.* [6] observe the easy axis to glide (zenithally) through an angle of 2.2° over the 150 hours during which the electric field is applied, increasing from its initial angle of 6.7° to 8.9°. On removal of the electric field, the easy axis direction glides back towards its initial position. After 13 days, its angle has decreased to 7.3° (0.6° larger than its value before the electric field was first applied). Joly *et al.* [6] state that anchoring is "strong" at this gliding boundary but do not provide precise values for anchoring strength, only a lower bound on the anchoring extrapolation length at that boundary. In the absence of firm data, we take $\mathcal{A}_0 = 1500$ for the dimensionless anchoring strength at the gliding boundary, an order of magnitude larger than the lower bound suggested by their estimate.

Based on the values reported in [6, 23, 24], we solve our models with the following parameter values: $h^* = 1.5$ μm, $\varepsilon_\parallel - \varepsilon_\perp \sim 5$ for the dielectric coefficient, giving $\mathcal{D} = 69$ when $E^* = 5V\mu\text{m}^{-1}$. In both gliding Models I & II (Eq. (26) and Eq. (27) respectively), we use the parameters α_{tol}, $\bar{\alpha}_{\text{tol}}$ and n (α_{tol} and n in Model I and $\bar{\alpha}_{\text{tol}}$ in Model II) to fit the experimental results shown in [6]. The goal of the remaining section is to determine which values of n and α_{tol} (for Model I) and $\bar{\alpha}_{\text{tol}}$ (for Model II) most accurately describe the experimental results. These are the optimal parameters denoted by $\alpha_{\text{tol}}^{\text{opt}}$, n^{opt} and $\bar{\alpha}_{\text{tol}}^{\text{opt}}$ respectively.

B. Comparison of numerical results with data of Ref. [6]

We solve Eqs. (20)–(22) in conjunction with Eq. (26) (Model I) and Eq. (27) (Model II) to obtain the evolution of the anchoring angle, $\alpha_0(t^*)$, at the gliding substrate, and the director angle, $\theta(0,t^*)$ there. We quantify how well each model predicts the gliding behavior observed in [6] by introducing $||\theta_{\rm exp}-\theta_{\rm num}||_2$ defined as:

$$||\theta_{\rm exp}-\theta_{\rm num}||_2=\sqrt{\int_{t_0}^{t_1}(\theta_{\rm exp}-\theta_{\rm num})^2dt} \qquad (28)$$

which denotes the norm of the difference between the experimental data and the numerical results. In each model, the norm is calculated for both gliding scenarios: (a) when the electric field is turned on and (b) after it is turned off. In each scenario, plots of $||\theta_{\rm exp}-\theta_{\rm num}||_2$ vs. $\alpha_{\rm tol}$ (not shown here) demonstrate that there exists an optimal value of $\alpha_{\rm tol}$ (for each n-value; Model I), or $\bar{\alpha}_{\rm tol}$ (Model II) that produces the best global fit i.e., the gliding curve with the lowest error. We denote these optimal values by $\alpha_{\rm tol}^{\rm opt}$, $\bar{\alpha}_{\rm tol}^{\rm opt}$ respectively. In what follows, we discuss the numerical results obtained from each model in detail.

1. *Gliding Model I: Eq. (26)*

We investigate the model behavior as parameters $\alpha_{\rm tol}$ and n are varied. As discussed in Section III A above, the values of several model parameters have already been fixed. The remaining parameter, the relaxation rate λ_0^*, is obtained by fitting the early time behavior: we take $\lambda_0^*=0.15$ hr^{-1} when the electric field is turned on, and $\lambda_0^*=20$ hr^{-1} when the electric field is turned off; the values of $\alpha_{\rm tol}$ and n mainly affect the intermediate-to-late time behavior.

Figure 6 presents the lowest norm, $\min||\theta_{\rm exp}-\theta_{\rm num}||_2$, for each n, versus the value of $\alpha_{\rm tol}$ giving this minimum, both when an electric field is applied (results shown by black symbols) and after the electric field is shut off (red symbols). We observe that the minimized error, $\min||\theta_{\rm exp}-\theta_{\rm num}||_2$, decreases as n increases, for both electric field on and off cases. Hence, we can conclude that highly nonlinear models (high values of n in Eq. (26)) better describe the gliding behavior in both electric field on and off scenarios.

The fitting procedure described above assumes both $\alpha_{\rm tol}$ and n can be varied independently to obtain optimal results in the field-on and field-off cases. However the results in Fig. 6 show that in fact there exist "optimal" modeling scenarios with $||\theta_{\rm exp}-\theta_{\rm num}||_2<0.1$ in both electric field *on* and *off* gliding scenarios, with the value of $\alpha_{\rm tol}$ fixed. For example, setting $\alpha_{\rm tol}\approx 4.3°$ together with $n=6$ (electric field on) and $n=11$ (electric field off) leads to a gliding curve with error norm $||\theta_{\rm exp}-\theta_{\rm num}||_2=0.06$, for both electric field *on* and *off* cases. Similar gliding curves with slightly higher errors (norm values) can be obtained by setting $\alpha_{\rm tol}^{\rm opt}=2.0°$ and $2.6°$ (and their corresponding values of n, seen in Fig. 6). Note that we choose to restrict n to integer values in Model I.

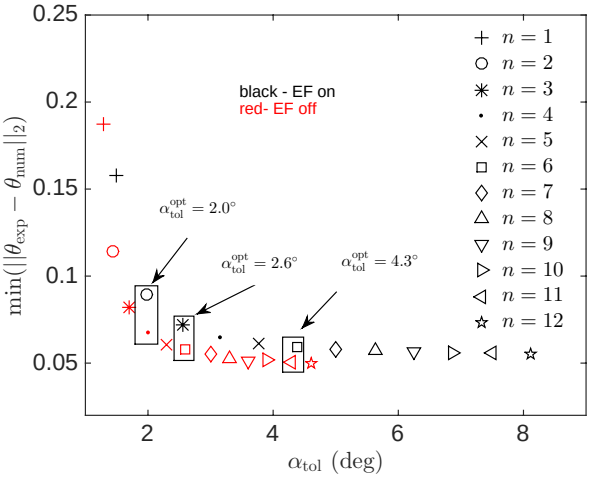

Figure 6: (Color online) The error $\min(||\theta_{\rm exp[5]}-\theta_{\rm num}||_2)$ vs $\alpha_{\rm tol}$ for electric field *on* and electric field *off* scenarios using Model I and the data of [6]. Each data point represents different n values.

A similar conclusion can be reached when fixing n and varying $\alpha_{\rm tol}$. Figure 7 illustrates the minimized error, $\min||\theta_{\rm exp}-\theta_{\rm num}||_2$, vs. n for the two gliding scenarios of Joly *et al.* [6] (the values of $\alpha_{\rm tol}^{\rm opt}$ that give the lowest norm are not shown in the figure) . We observe that in both gliding scenarios, as the value of n increases, the minimum error decreases, reaching a plateau value of less than 0.06 at large n. We obtain the best fit to the experimental data when $n=12$ and $\alpha_{\rm tol}=8.12°$ for the electric field *on* case, and $n=12$ and $\alpha_{\rm tol}=4.6°$ for the electric field *off* case (see Eq. (26)). As in the previous scenario, the lowest error is achieved by a highly nonlinear model (Eq. (26) with $n=12$; though in fact any $n\geq 5$ gives an acceptably small error). Figures 6 and 7 illustrate that we do not need to vary two parameters $\alpha_{\rm tol}$ and n independently to obtain a good global fit to the experimental data observed in [6]. Moreover, they show that higher values of n lead consistently to better descriptions of the experimental data.

2. *Gliding Model II: Eq. (27)*

Motivated in part by the strong nonlinearity suggested by the results just described, we now investigate how Model II (given by Eq. (27)) predicts the experimental data observed by [6]. This model has the advantage of only one variable parameter, $\bar{\alpha}_{\rm tol}$. This parameter represents a threshold below which gliding follows a linear model and above which the torque driving gliding drops

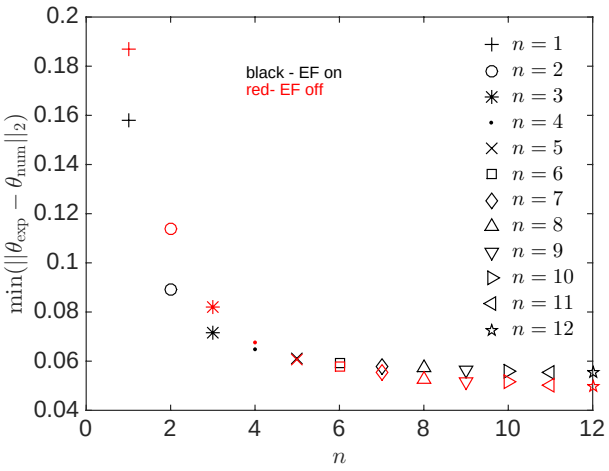

Figure 7: (Color online) The error $||\theta_{\exp[5]} - \theta_{\rm num}||_2$ vs n for electric field *on* and electric field *off* scenarios using Model I and the data of [6]. Each data point represents a minimum obtained over all relevant $\alpha_{\rm tol}$ values (the minimizing values of $\alpha_{\rm tol}$ are not shown here).

rapidly, and we enter a strongly nonlinear regime. As with Model I, we quantify how well the numerical results compare with the experimental data by varying the parameter $\bar{\alpha}_{\rm tol}$ and measuring the error between the experimental data and numerical results, $||\theta_{\rm exp} - \theta_{\rm num}||_2$ (defined in Eq. (28)).

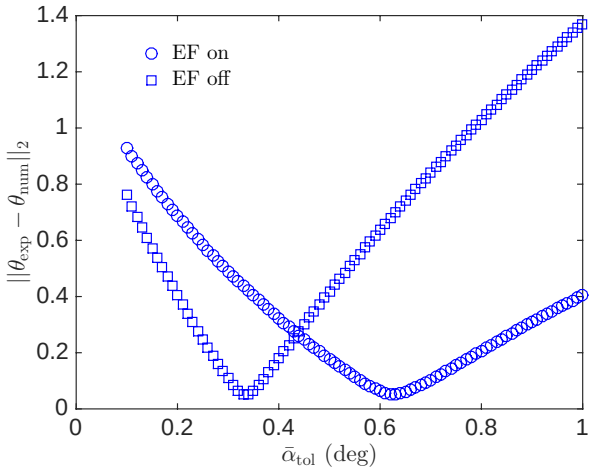

Figure 8: (Color online) The error $||\theta_{\exp[5]} - \theta_{\rm num}||_2$ vs $\bar{\alpha}_{\rm tol}$ for electric field *on* and electric field *off* scenarios using Model II and the data of [6].

Figure 8 presents the norm $||\theta_{\rm exp} - \theta_{\rm num}||_2$ as $\bar{\alpha}_{\rm tol}$ varies. We observe that in both gliding scenarios there exists an optimal value of $\bar{\alpha}_{\rm tol}$, $\bar{\alpha}_{\rm tol}^{\rm opt}$, such that $||\theta_{\rm exp} - \theta_{\rm num}||_2$ is minimized. In the electric field *on* case, $\bar{\alpha}_{\rm tol}^{\rm opt} = 0.63°$ (resulting in $||\theta_{\rm exp} - \theta_{\rm num}||_2 < 0.06$); while in the electric field *off* case, $\bar{\alpha}_{\rm tol}^{\rm opt} = 0.33°$ (giving $||\theta_{\rm exp} - \theta_{\rm num}||_2 < 0.05$). Note that Model II is able to describe the experimental data observed in [6] as accurately as Model I with only one variable parameter: in both gliding scenarios, the error norm $||\theta_{\rm exp} - \theta_{\rm num}||_2 < 0.06$, similar to Model I.

3. *Comparison of models with experimental data*

We now illustrate how the best fits for the two models, obtained as described above, compare to the experimental results of Joly *et al.* [6]. Figure 9 shows the gliding evolution of $\theta(0, t^*)$ using Model I (solid black line) and Model II (dashed red line) plotted on the same axis as the gliding data obtained in [6] (a) when an electric field is turned on and (b) after the electric field is turned off. Experimental data were extracted from [6] (and later from [10, 12]) using Data Thief III (Ref. [25]). In both cases we convert our model results to show evolution in dimensional time (hours), since that is how the experimental data are presented in the original work. In the electric field *on* scenario, we use $n = 12$ and $\alpha_{\rm tol} = 8.12°$ to obtain the best fit with Model I and we use $\bar{\alpha}_{\rm tol} = 0.63°$ to obtain the best fit with Model II. After the electric field is turned *off*, the best gliding fit is obtained using $n = 12$ and $\alpha_{\rm tol} = 4.6°$ for Model I and $\bar{\alpha}_{\rm tol} = 0.33°$ for Model II; these parameters produce gliding curves with the lowest error: $||\theta_{\rm exp} - \theta_{\rm num}||_2 < 0.06$ in all cases. We observe that our numerical results provide an excellent fit to the gliding evolution observed in [6], with gliding Model II (Eq. (26)) performing slightly better than gliding Model I (Eq. (27)).

C. Overview of experimental results presented in Ref. [10]

Buluy *et al.* [10] consider a set up similar to that of Joly *et al.* [6]. A layer of 5CB is bounded between two parallel plates, 10 μm apart, treated such that only the lower substrate exhibits gliding. The initial preferred anchoring orientation is measured to be $\alpha_0 = 0.8°$ from the horizontal axis, with anchoring strength $\mathcal{A}_0^* \sim 0.25 \times 10^{-3} \mathrm{Jm}^{-2}$, corresponding to $\mathcal{A}_0 = 312$ (Eq. (12) with $h = 10$ μm). An electric field of magnitude $1 \mathrm{V}\mu\mathrm{m}^{-1}$ is applied perpendicularly to the substrate for a period of 16 hours, during which gliding occurs. The field is then removed and the new easy axis orientation is measured: 3.0°. The easy axis then begins to glide back towards its original orientation, and its evolution is tracked over a period of 1000 hours.

D. Comparison of numerical results with data of Ref. [10]

We use a similar approach to Section III B where we compare the experimental results obtained in [10] un-

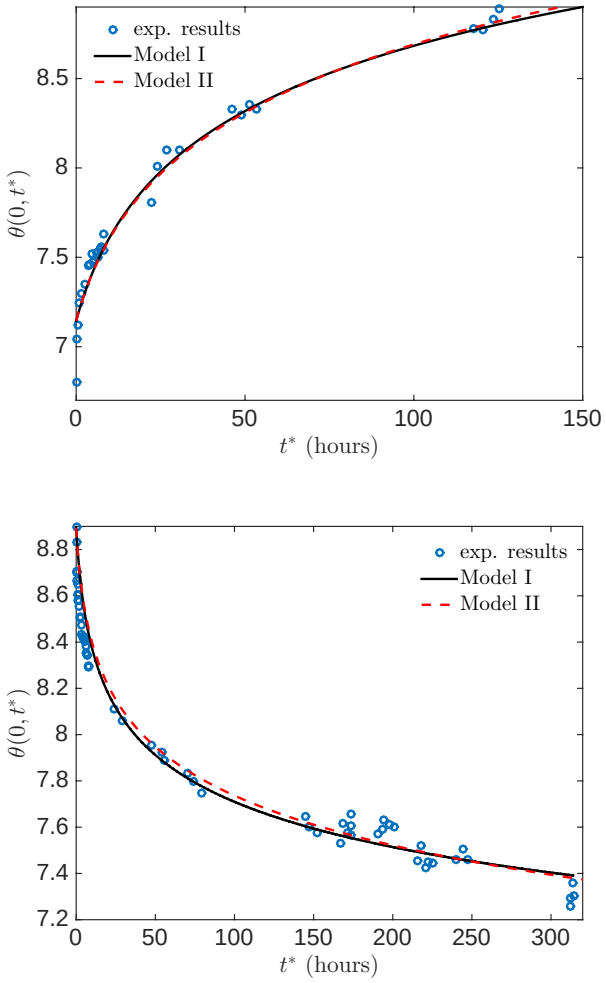

Figure 9: (Color online) Experimental results [6] (blue circles) and the results for $\theta(0,t^*)$ using Models I (solid black line) & II (dashed red line) when the electric field is (a) *on* and (b) *off*. Parameters used to obtain the numerical results using Model I are: (a) $\lambda_0^* = 0.15$ hr^{-1}, $n = 12$, $\alpha_{\rm tol} = 8.12°$ and (b) $\lambda_0^* = 20$ hr^{-1}, $n = 12$, $\alpha_{\rm tol} = 4.6°$. Parameters used to obtain the numerical results using Model II are: (a) $\lambda_0^* = 0.15$ hr^{-1}, $\bar{\alpha}_{\rm tol} = 0.63°$ and (b) $\lambda_0^* = 20$ hr^{-1}, $\bar{\alpha}_{\rm tol} = 0.33°$.

der zenithal gliding with the numerical results obtained by solving Eqs. (20)–(22) in conjunction with Eq. (26) (Model I) or Eq. (27) (Model II). We use the technique described at the end of Section II D to obtain the gliding evolution of $\theta(0,t^*)$ using the following parameters: $\mathcal{A}_0 = 312$, $\alpha_0(0) = 0.8°$, $\mathcal{D} = 0$ (in [10] the authors only present data for the gliding after the electric field has been removed, so we are only able to compare our model for this regime). As with the experimental data in [6] (see Sec. III B 1) the relaxation rate λ_0^* is obtained by fitting the early time behavior of the numerical results to the experimental data and it is set to $\lambda_0^* = 3.7$ min^{-1}.

1. *Gliding Model I: Eq. (26)*

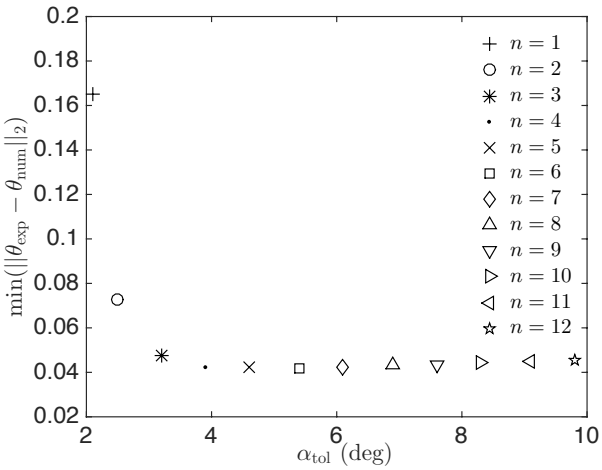

Figure 10: (Color online) The error $\min(||\theta_{\exp[9]} - \theta_{\rm num}||_2)$ vs $\alpha_{\rm tol}$ for electric field *off* using Model I and the data of [10]. Each data point represents different n values.

We investigate the numerical results obtained by solving Eqs. (20)–(22) together with Eq. (26) and observe (as in Sec. III B) that for each value of n, there exists an optimal value of $\alpha_{\rm tol}$, $\alpha_{\rm tol}^{\rm opt}$, that produces the best global fit to the experimental data. Figure 10 shows the smallest error, $\min||\theta_{\rm exp} - \theta_{\rm num}||_2$ plotted against the corresponding value of $\alpha_{\rm tol}$, for different integers n. We observe that as n increases, the error between the numerical results and experimental data decreases at first (when $n < 6$), reaching its lowest value ($||\theta_{\rm exp} - \theta_{\rm num}||_2 < 0.05$) when $n = 6$ (and $\alpha_{\rm tol} = 5.4°$), followed by a slight increase when $n > 6$. Hence, we conclude that the parameters $n = 6$ and $\alpha_{\rm tol} = 5.4°$ in Model I lead to the best global approximation of the experimental results reported in Ref. [10] with an error $||\theta_{\rm exp} - \theta_{\rm num}||_2 < 0.05$. Note that, as with the zenithal gliding data reported in [6], a highly nonlinear model ($n = 6$ and $\alpha_{\rm tol} = 5.4°$) is needed to best fit the experimental data observed in [10].

2. *Gliding Model II: Eq. (27)*

We now investigate whether Model II given by Eq. (27) can better describe the gliding data observed in [10]. Figure 11 shows the norm of the difference between numerical and experimental results plotted against $\bar{\alpha}_{\rm tol}$. Here, as in Fig. 8, we observe that there exists an optimal value of $\bar{\alpha}_{\rm tol}$, $\bar{\alpha}_{\rm tol}^{\rm opt} = 0.75°$ such that $||\theta_{\rm exp} - \theta_{\rm num}||_2$ is minimized ($||\theta_{\rm exp} - \theta_{\rm num}||_2 < 0.08$). Note that although Model II (Eq. (27)) leads to a slightly "worse" prediction with $||\theta_{\rm exp} - \theta_{\rm num}||_2 \approx 0.079$ than Model I (with $||\theta_{\rm exp} - \theta_{\rm num}||_2 < 0.05$ when $n = 6$ and $\alpha_{\rm tol} = 5.4°$), it requires only a single fitting parameter, $\bar{\alpha}_{\rm tol}$.

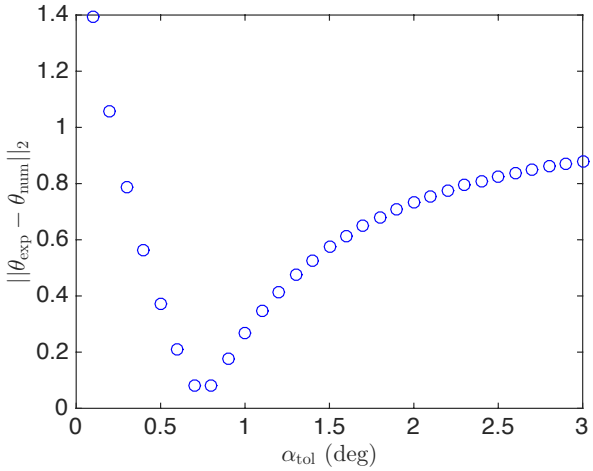

Figure 11: (Color online) The error $||\theta_{\rm exp[9]} - \theta_{\rm num}||_2$ vs $\bar{\alpha}_{\rm tol}$ for electric field *off* scenario using Model II and the data of [10].

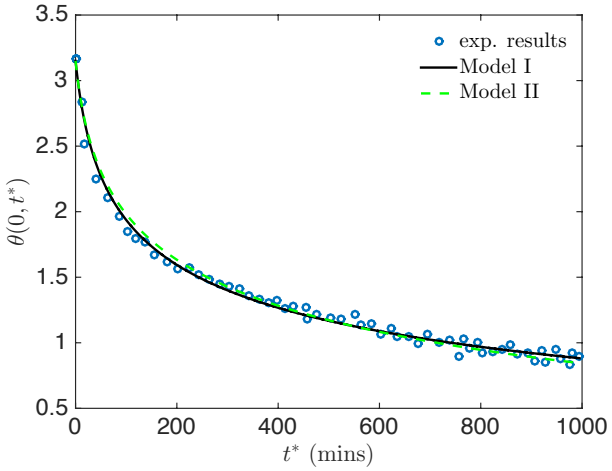

Figure 12: (Color online) Evolution of $\theta(0,t^*)$ using Models I (solid black line) & II (dashed green line) and the experimental data of [10] (blue circles; obtained after the electric field is turned off). Parameters for Model I are: $\lambda_0^* = 3.7$ min^{-1}, $n = 6$ and $\alpha_{\rm tol} = 5.4°$; and for Model II, $\lambda_0^* = 3.7$ min^{-1}, $\bar{\alpha}_{\rm tol} = 0.75°$.

3. *Comparison of models with experimental data*

We now illustrate how the best numerical results for both models compare to the experimental data of [10]. Figure 12 shows the gliding evolution of $\theta(0,t^*)$ using Model I (solid black line) and Model II (dashed green line) plotted on the same axis as the gliding data (again we convert our simulation results to dimensional time, measured in minutes). The best fit for Model I is obtained when $n = 6$ and $\alpha_{\rm tol} = 5.4°$; while for Model II it is obtained when $\bar{\alpha}_{\rm tol} = 0.75°$. These parameters lead to gliding curves with the lowest error: $||\theta_{\rm exp} - \theta_{\rm num}||_2 < 0.05$ (Model I) and $||\theta_{\rm exp} - \theta_{\rm num}||_2 < 0.08$ (Model II). We observe that each model provides an excellent fit to the gliding evolution shown in [10], with gliding Model I (Eq. (27)) performing slightly better than gliding Model II (Eq. (26)).

E. Overview of experimental results presented in Ref. [12]

The experiment considered by Faetti & Marianelli in [12] consists of a slightly different setup, designed to induce azimuthal gliding of the easy axis: a wedge cell containing NLC is bounded between two substrates treated such that they both exhibit gliding. The initial preferred anchoring orientation at each boundary is $\beta_{\{0,1\}} = 0°$, measured from the x^*-axis (see Figure 5 and Eqs. (23)–(25)). Faetti & Marianelli state that anchoring is "strong" at both boundaries with anchoring strength values around $\mathcal{B}^*_{\{0,h^*\}} \sim 0.33 \times 10^{-3}$ Jm^{-2}. An electric field of magnitude 0.25 $V\mu$m^{-1} is applied parallel to the lower plate, at an angle 85° from the x-axis.

Based on the reported data [12] we solve our model with the following parameter values: $h^* = 75$ μm, $\varepsilon_\parallel - \varepsilon_\perp \sim 13.1$, $K^* = 3.93 \times 10^{-12}$ N, $\mathcal{B}^*_{\{0,h^*\}} \sim 0.33 \times 10^{-3}$ Jm^{-2}, and obtain $\mathcal{B}_{\{0,1\}} = 4500$ and $\mathcal{D} = 5188$ for the dimensionless anchoring strength and dielectric coefficient respectively when $E^* = 0.25$ $V\mu$m^{-1}.

As the electric field is turned on, Faetti & Marianelli [12] initially report a jump of the easy axis from 0° to 1.4° from the x-axis in the first two minutes followed by a gradual increase to 1.9° over approximately 60 minutes. We attribute the initial jump to the response of the NLC molecules to the electric field, and the subsequent gradual increase to gliding.

F. Comparison of numerical results with data of Ref. [12]

For these experimental data we present only results obtained from Model II (Eqs. (23)–(25) plus Eq. (27)), since Model I proves less satisfactory here. Given the parameters $\mathcal{B}_0 = 4500$, $\beta_0(0) = 0°$, $\mathcal{D} = 5188$, determined in Sec. III E above, we obtain very good agreement with the data using the value of $\bar{\beta}_{\rm tol}$ that minimizes $||\phi_{\rm exp} - \phi_{\rm num}||_2$ (as with our previous examples, the value of λ_0^* is obtained by fitting the early time behavior of the numerical results to the experimental data: $\lambda_0^* = 0.275$ min^{-1}).

Figure 13 illustrates the well-defined minimum of the error $||\phi_{\rm exp} - \phi_{\rm num}||_2$ (defined as in Eq. (28)), obtained at $\bar{\beta}^{\rm opt}_{\rm tol} = 0.1°$. Figure 14 shows the direct comparison of numerical results (red curve) and experimental data (blue circles, [12]) for this value of $\bar{\beta}_{\rm tol}$. We use the reported post-jump value, $\phi(0,0) = 1.4°$, as our initial condition, attributing the fast initial change to the initial response to the applied field, before any gliding occurs (such a

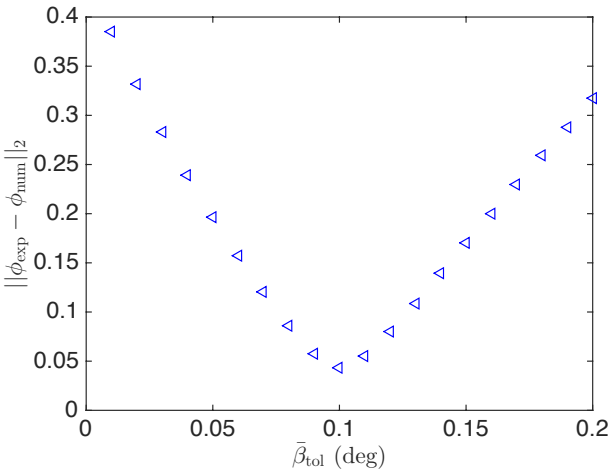

Figure 13: (Color online) The error $(||\phi_{\rm exp[11]} - \phi_{\rm num}||_2$ vs $\bar{\beta}_{\rm tol}$ for electric field *on* scenario using Model II and the data of [12].

jump in $\phi(0,0)$ would be observed even at a non-gliding surface, with finite anchoring strength). As with the previous cases considered, the fit obtained with Model II is excellent.

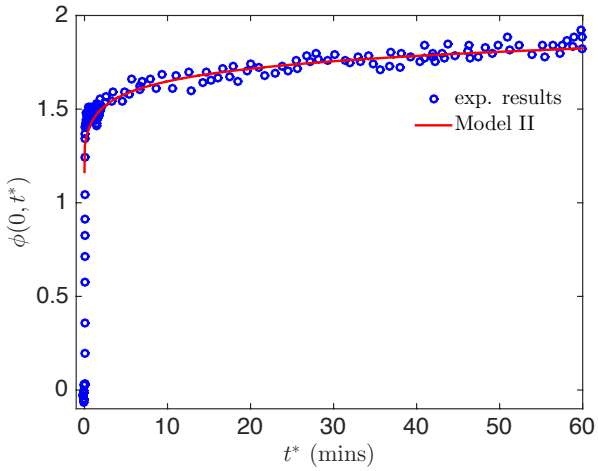

Figure 14: (Color online) Evolution of $\phi(0,t^*)$ using Model II (solid red line) and the experimental data of [12] (results obtained under an electric field applied at time $t^* = 0$). Parameters used to obtain the numerical results are: $\lambda_0^* = 0.275$ min^{-1} and $\bar{\beta}_{\rm tol} = 0.1°$.

IV. CONCLUSIONS

We present two simple models that describe the evolution of the director field within a NLC layer in the following scenarios: (i) when an electric field is applied perpendicularly to the plates and zenithal gliding occurs at one plate; and (ii) when an electric field is applied parallel to the plates and azimuthal gliding occurs at both plates. We investigate in detail the long term evolution of the easy axis on the gliding surface that occurs both when the layer is subjected to an electric field, and after the electric field is turned off. The models that we introduce are based on the assumption that the anchoring angles, α_0 (zenithal gliding) and β_0, β_1 (azimuthal gliding), reorient at a rate that depends on the difference between the anchoring angle and the surface director at the gliding surface. In Model I, given by Eq. (26), gliding persists until the anchoring angle has changed by a maximal amount, $\alpha_{\rm tol}$ (or $\beta_{\rm tol}$ in the azimuthal gliding case), or until the director takes the same value as the preferred anchoring angle at the boundary. In Model II, given by Eq. (27), we assume the existence of some angle $\bar{\alpha}_{\rm tol}$ ($\bar{\beta}_{\rm tol}$ for azimuthal gliding), below which gliding follows an approximately linear model, and above which the torque driving gliding drops rapidly. In each model, we take advantage of the separation of the time scales between gliding and the elastic response, and assume a quasistatic model to describe the evolution of the director field within the layer. We investigate in detail how the easy axis evolves in time under the two gliding models, and compare our numerical results with the experimental data observed in Ref. [6, 10, 12].

We observe that, given the appropriate parameter values, $\alpha_{\rm tol}(\beta_{\rm tol}), \lambda_0^*$ and n for each zenithal (azimuthal) experiment, both models predict the gliding data observed in [6, 10, 12] extremely well. Model I obtains a slightly better global fit to the data of [6, 10] (Sections III B, III D), but uses two fitting parameters (an exponent n characterizing the degree of nonlinearity, in addition to the limiting gliding angle). Model II performs only marginally worse in terms of overall error, with the advantage of only a single fitting parameter in the nonlinear regime. The fact that the optimal values for the fitting parameters are found to be different in field-on and field-off cases is attributed to the possible effect that the electric field has on the molecules of the polymeric bounding substrate itself. Since excellent overall fits are obtained to all datasets with this model, we suggest that Model II provides a simple, robust way in which to characterize director gliding, in the presence or absence of an electric field.

After this work was completed, another study by Antonova *et al.* [26] was brought to our attention. This study shares some similarities with those of [6, 10], in that the same basic experimental setup is considered (application of an electric field across a NLC layer with strong anchoring at one substrate and gliding at the other; the same polymer, PVCN-F, was used as in the experiments of Buluy *et al.* [10] at the gliding surface), and a triexponential function of the kind used by Joly *et al.* [6] is used to fit the data, again confirming the strong nonlinearity of the gliding response. Antonova *et al.* [26] however take the work further, repeating the experiment through several cycles of gliding to study the aging of

the system. Given that our simulations do not exhibit full reversibility (on removal of the electric field the easy axis does not return to its exact value before application of the field), our model has the potential to capture dynamically such system aging. It would be interesting in future to pursue this direction making direct comparison to the experimental data of [26].

V. ACKNOWLEDGMENTS

The authors gratefully acknowledge several helpful conversations with Peter Palffy-Muhoray of Kent State University. Helpful comments from the anonymous reviewers are also acknowledged. This work was supported by the NSF under grant DMS-1211713.

[1] E.A. Oliveira, A.M. Figueiredo Neto, and G. Durand, "Gliding anchoring of lyotropic nematic liquid crystals on amorphous glass surfaces," Phys. Rev. A **44**, R825–R827 (1991).

[2] I. Jánossy and T. I. Kósa, "Gliding of liquid crystals on soft polymer surfaces," Phys. Rev. E **70**, 052701 (2004).

[3] I. Jánossy, "Kinetics of director gliding on a polymer liquid-crystal interface," Phys. Rev. E **81**, 031714 (2010).

[4] S. V. Pasechnik, V. G. Chigrinov, D. V. Shmeliova, V. A. Tsvetkov, V. N. Kremenetsky, L. Zhijian, and A. V. Dubtsov, "Slow relaxation processes in nematic liquid crystals at weak surface anchoring," Liq. Cryst. **33**, 175–185 (2006).

[5] P. Vetter, Y. Ohmura, and T. Uchida, "Study of memory alignment of nematic liquid crystals on polyvinyl alcohol coatings," Jpn. J. Appl. Phys, Part 2: Letters **32**, L1239–L1241 (1993).

[6] S. Joly, K. Antonova, P. Martinot-Lagarde, and I. Dozov, "Zenithal gliding of the easy axis of a nematic liquid crystal," Phys. Rev. E **70**, 050701 (2004).

[7] V. P. Vorflusev, H. Kitzerow, and V. G. Chigrinov, "Azimuthal surface gliding of a nematic liquid crystal," Appl. Phys. Lett. **70**, 3359–3361 (1997).

[8] S. V. Pasechnik, A. V. Dubtsov, D. V. Shmeliova, D. A. Semerenko, V. G. Chigrinov, M. A. Sinenko, and A. D. Kiselev, "Modeling reorientation dynamics of electrically assisted light-induced gliding of nematic liquid-crystal easy axis," Adv. Cond. Matter Phys. **2013**, 363157 (2013).

[9] J. H. Lee and T. H. Yoon, "P-77: Image sticking in a flexible liquid crystal display stabilized with polymers: Surface gliding effect," SID Int. Sym. Dig. Tec. **43**, 1343–1345 (2012).

[10] O. Buluy, A. Iljin, E. Ouskova, Y. Reznikov, C. Blanc, M. Nobili, and K. Antonova, "Anchoring and gliding of easy axis of 5CB on photoaligning PVCN-F surface," J. Soc. Inf. Disp. **14**, 603–610 (2006).

[11] Y. Kurioz, V. Reshetniak, and Y. Reznikov, "Orientation of a liquid crystal on a soft photoaligning surface," Mol. Cryst. Liq. Cryst. Sci. Technol., Sect. A **375**, 535–541 (2002).

[12] S. Faetti and P. Marianelli, "Azimuthal director gliding at a strongly anchoring interface of polyimide," Liq. Cryst. **33**, 327–334 (2006).

[13] L. J. Cummings, E. Mema, C. Cai, and L. Kondic, "Electric-field variations within a nematic-liquid-crystal layer," Phys. Rev. E **90**, 012503 (2014).

[14] J. L. Ericksen, "Theory of anisotropic fluids," J. Rheol. **4**, 29–39 (1960).

[15] F. M. Leslie, "Some constitutive equations for anisotropic fluids," Q. J. Mech. Appl. Math **19**, 357–370 (1966).

[16] F. M. Leslie, "Some constitutive equations for liquid crystals," Arch. Rational Mech. Anal. **28**, 265–283 (1968).

[17] L. J. Cummings, C. Cai, and L. Kondic, "Towards an optimal model for a bistable nematic liquid crystal display device," J. Eng. Math. **80**, 21–38 (2013).

[18] L. J. Cummings and G. Richardson, "Bistable nematic liquid crystal device with flexoelectric switching," Eur. J. Appl. Math **17**, 435–463 (2006).

[19] P. J. Kedney and F. M. Leslie, "Switching in a simple bistable nematic cell." Liq. Cryst. **24**, 613–618 (1998).

[20] S. Faetti, M. Nobili, and I. Raggi, "Surface reorientation dynamics of nematic liquid crystals," Eur. Phys. J. B **11**, 445–453 (1999).

[21] I. Jánossy, "High-precision measurement of azimuthal rotation of liquid crystals on solid substrates," J. App. Phys. **98**, 043523 (2005).

[22] E. Mema, L. Kondic, and L. J. Cummings, "Substrate-induced gliding in a nematic liquid crystal layer," Phys. Rev. E **92**, 062513 (2015).

[23] A. J. Davidson and N. J. Mottram, "Flexoelectric switching in a bistable nematic device," Phys. Rev. E **65**, 051710 (2002).

[24] A. Buka and N. Éber, *Flexoelectricity in Liquid Crystals: Theory, Experiments and Applications* (Imperial College Press, London, UK, 2013).

[25] "Data thief III," `http://datathief.org` (2015), (Accessed on November 28, 2016).

[26] K. Antonova, K. Slyusarenko, O. Buluy, C. Blanc, S. Joly, Y. Reznikov, and M. Nobili, "Aging in glassy polymer-liquid-crystal layers," Phys. Rev. E **83**, 050701 (2011).